Skin-Integrated Electromechanical Systems for Characterization of Deep Tissue Biomechanics

John Rogers (jrogers@northwestern.edu)
Northwestern University https://orcid.org/0000-0002-2980-3961

Enming Song
Northwestern University https://orcid.org/0000-0002-2658-904X

Zhaoqian Xie
Dalian University of Technology https://orcid.org/0000-0003-1320-817X

Wubin Bai
Querrey Simpson Institute for Bioelectronics, Center for Bio-integrated Electronics, Northwestern University, Evanston, IL

Haiwen Luan
Querrey Simpson Institute for Bioelectronics

Bowen Ji
Northwestern Polytechnical University

Xin Ning
Pennsylvania State University

Yu Xia
University of Illinois at Urbana-Champaign

Janice Mihyun Baek
Department of Chemistry University of Illinois at Urbana-Champaign Urbana, IL

Yujin Lee
Department of Chemistry University of Illinois at Urbana-Champaign Urbana, IL

Raudel Avila
Northwestern University

Huang-Yu Chen
Northwestern University

Jae-Hwan Kim
Frederick Seitz Materials Research Laboratory, University of Illinois at Urbana–Champaign Urbana, IL

Surabhi Madhvapathi
Northwestern University

Kuanming Yao
City University of Hong Kong

Sang Won
Sungkyunkwan University

Xinyuan Zhang
Fudan University
Daniel Myers
Northwestern University
Yongfeng Mei
Fudan University
Xu Guo
Dalian University of Technology
Shuai Xu
Northwestern University
Xinge Yu
City University of Hong Kong https://orcid.org/0000-0003-0522-1171
Yonggang Huang
Northwestern University https://orcid.org/0000-0002-0483-8359

Article

Keywords: deep tissue biomechanics, skin disorders, skin-Integrated electromechanical systems

Posted Date: December 31st, 2020

DOI: https://doi.org/10.21203/rs.3.rs-134565/v1

Version of Record: A version of this preprint was published at Nature Biomedical Engineering on May 27th, 2021. See the published version at https://doi.org/10.1038/s41551-021-00723-y.

Abstract

Compact electronic systems that perform rapid, precise mechanical characterization of living biological tissues have important potential uses in monitoring and diagnosing various types of human-health disorders. Active devices that perform high-precision, real-time evaluations of deep tissue structures (millimeter-scale) in a precise, digital and non-invasive fashion could complement capabilities of recently-reported approaches for sensing tissue biomechanics at superficial depths (typically micrometer-scale). This paper introduces a miniature electromagnetic platform that combines a vibratory actuator with a soft strain-sensing sheet for determining the Young's modulus of soft biological tissues, with specific focus on skin. Experimental and computational studies establish the operational principles and performance attributes through evaluations of synthetic and biological materials, including human skin at various body locations across healthy subject volunteers. The results demonstrate dynamic monitoring of elastic modulus at characteristic depths between ~1 and ~8 mm, depending on the sensor designs. Arrays of such devices support capabilities in both depth profiling and spatial mapping. Clinical studies on patients with skin disorders highlight potential for accurate targeting of lesions associated with psoriasis, as examples of practical medical utility.

Introduction

Technologies for rapid, *in vivo* assessments of soft tissue biomechanics have potential for broad utility in biological research and clinical diagnostics[1,2]. Of particular interest are advanced electromechanical systems that enable precise measurements of mechanical properties of tissues[3] that can provide diagnostic utility, track response to treatment and evaluate for small but clinically meaningful deterioriation for a wide range of dermatological conditions. For example, characterization of soft tissue biomechanics may guide objective assessment of disease severity for edema associated with lower venous leg disorders[4] or scleroderma, a lethal rheumatological and dermatological disease that currently depends on subjective physician grading scales[5]. An important focus is on the elastic modulus (the relationship between strain and stress), as the basis for dermatological evaluations of these diseases[1]. Additional possibilities are in tracking of wound healing cascades and in tissue growth, regeneration and aging, each of which involves changes in the elastic modulus of the surface and/or sub-surface layers[6-9]. Conventional methods for characterization rely on quasi-static measurements of displacement as a function of applied forces delivered via suction, torsion, compression or indentation[10-15]. An alternative known as magnetic resonance elastography (MRE) provides quantitative measurements of elastic modulus, including spatial-temporal mapping of tissue stiffness[16,17]. Although useful in many scenarios, these techniques usually involve elaborate setups and trained practitioners, as barriers to use outside of hospital and laboratory settings. Also, in many cases, the required tissue interfaces can lead to measurement uncertainties and difficulties in mounting on curved or textured surfaces to track time-dependent changes in mechanical properties.

Due to their miniature dimensions and skin-compatible formats, emerging classes of bio-integrated electronic platforms may offer powerful alternatives[18,19]. Recent research establishes the use of thin, flexible piezoelectric actuators and/or sensors for characterization of soft tissue biomechanics, with measurements that rely on minute deformations of tissues at near-surface regions. Examples range from conformal sheets for high-resolution mapping of the elastic modulus near the surfaces of skin lesions[20], to needle-shaped penetrating probes for *in vivo* mechanical sensing as guidance in biopsies[21], and to thin, flexible piezoresistive cantilevers as indentation sensors for mechanical characterization of cancerous breast tissues[3]. These and other related platforms differ from past technologies in their thin, flexible geometries and their ability to form minimally invasive interfaces to complex topographies and textures of biological surfaces[22-24]. An important mode of use is in locating and identifying aberrant tissues through abnormal elastic moduli that result from specific disease states[3,20,21,25]. In many cases, however, the limited depth of sensing and the complex designs of these devices represent drawbacks that prevent uses in many important applications.

This paper presents a simple, miniature electromechanical system that can interface with biological tissues for rapid evaluations of their elastic modulus, at a range of frequencies and depths and across a variety of spatial scales, including two dimensional mapping. These devices integrate components for mechanical actuation and sensing in a single package, using certain ideas adapted from those used as the basis of skin-integrated haptic interfaces for virtual/augmented reality[26]. The following describes the engineering concepts, with a focus on measurements of elastic moduli of biological targets averaged over depths that are tunable across the millimeter range. Experimental and simulation studies demonstrate quantitative measurements of tissue modulus for a wide scope of coupling substrates and conditions, including bilayer test structures as illustrations of depth profiling. Examples range from mechanical evaluations of biomaterials (hydrogels) with moduli comparable to those of soft human tissues, to samples of skin from animal models, to various locations on human subject volunteers. The results define some envisioned applications, including those relevant to clinical evaluations on patients with skin disorders. Advanced versions incorporate arrays of such devices for large-area mapping of elastic modulus. These findings have broad potential for use in exploratory research, clinical medicine and at-home diagnostics.

Results And Discussion

Materials, designs, integration schemes and performance characteristics. Fig. 1a presents a schematic illustration and an image of a representative device, which we refer to as an electromechanical modulus (EMM) sensor. The stack involves (1) a top layer that generates a time-dependent Lorenz force, as the source for vibratory actuation (Fig. 1b), (2) a thin strain sensor in the form of a serpentine metal trace, as the basis for mechanical sensing (Fig. 1c) and (3) a supporting thin elastomeric layer, as a reversible, soft interface to a tissue surface. The total thickness of this example is 2.5 mm and the contacting area is ~2 cm^2 (lower inset of Fig. 1a). The fabrication begins with patterning of serpentine-shaped electrical traces as resistive strain sensors, followed by transfer printing onto a soft, flexible substrate

(poly(dimethylsiloxane) (PDMS), ~30 μm thick). Thin gold (Au) lines form an open mesh structure (100 nm thick) to define a sensing area of ~0.5 cm^2, embedded above and below by layers of polyimide (1 μm thick), as illustrated in Figs 1c and d. A sequence of assembly steps prepares the actuator and wired connections for integration with the underlying sensor to yield a functional system. The actuator includes a nickel-coated neodymium magnet (8 mm diameter, 1.5 mm thick) on a thin polyimide disk (75 μm thick) and a copper coil (Cu, 50 μm wire diameter, 240 turns with an outer diameter of 12 mm, electrical resistance of ~70 Ohm (Yisu Electronics, Inc.)), as displayed in Fig. 1b. Detailed information appears in the Supplementary Figs 1 and 2.

As illustrated in the equivalent circuit diagram in the upper inset of Fig. 1a, the magnet undergoes vibratory motions upon application of alternating current through the copper coil (V_A; < 5 V, sine-wave, 50 Hz), with a travelling amplitude of several hundreds of micrometers (Supplementary Movie 1). The ring-shaped shell (PDMS, 2.4 mm thick) around the actuator defines space for out-of-plane motions of the magnet, thereby creating forces on the contacting tissues under test due to inertial effects (Fig. 1a) and directed deformations that extend to millimeter-scale depths of tissue. The result yields strains distributed over the metal traces of the strain sensor, thus leading to periodic variations in the electrical resistance. Analysis of these responses by simultaneous measurements of the voltage across the strain sensor (output voltage, V_S) via lock-in techniques (SR830, Stanford Research Systems) allows quantitative determination of the elastic modulus of the tissues. Specifically, a constant current (I_S) delivered from a current source to the strain sensor (Fig. 1d and Supplementary Fig. 2) provides an input channel to the lock-in amplifier, to capture the amplitudes of periodic variations in the sensor resistance, as V_S at the frequency of the vibration. By comparison to existing methods for sensing tissue biomechanics at superficial depths (micrometer-scale) by use of piezoelectric actuators/sensors[20,21], these devices mechanically couple with contacting tissues through millimeter-scale thicknesses and thereby allow characterization of deep tissue biomechanics on length scales defined by the geometry of the sensor, as described subsequently. Information on the measurement mechanism and operational principles appear in Supplementary Fig. 3.

The surface of the strain sensor allows intimate, stable interfaces to tissues of interest (*i.e.* forearm, Fig. 1e). Conformal contact occurs via lamination in a simple, reversible manner that enables multiple cycles of use (100×), without significant change in measurement accuracy (Fig. 1e and Supplementary Fig. 4). Fig. 1f shows a device conformally mounted on the curved surface of the skin of the fingertip of a volunteer subject. As shown in Supplementary Fig. 5a, the performance remains the same, to within experimental uncertainties, after 10^3 cycles of bending into cylindrical shapes. The encapsulation layers (polyimide/PDMS, 1 μm/30 μm thick)[27] isolate the system from moisture or biofluids. Specifically, the devices offer consistent performance before and after 7 days of immersion in artificial sweat solution at 50 ^oC (Supplementary Fig. 5b). With the actuator mounted on top, the devices offer stable measurement results on curved surfaces with different radii of curvature (Fig. 1g and Supplementary Fig. 6).

These simple designs and fabrication strategies yield reliable devices at high yields. Statistical data for the resistance of the strain sensor (R_{sensor}), the device yield and the signal-to-noise ratio (*SNR*) associated with 100 devices appear in Supplementary Fig. 7. The yield corresponds to the percentage of functional devices, and the *SNR* is the ratio between V_S and the noise level with a sine wave with amplitude, V_A, of 5V at a frequency, *f*, of 50 Hz in the top actuator, during measurements. Failure most typically results from fractures in the strain sensor or from disconnections between the wires of the coil in the actuator. These results suggest high levels of uniformity and consistency in device performance (*e.g.* R_{sensor} ~10^3 Ohm, total yield 96 % and *SNR* ~ 40 dB). Although this system can apply to a range of biological tissues, the results reported here focus on human skin through studies of healthy volunteers (Fig. 1g) and patients associated with a dermatology clinic, on various body locations, including curved surfaces of the face, forearm, shoulder, *etc* (Supplementary Fig. 8).

Experimental and computational analysis of the device operation. For a given V_A and *f*, the magnet responds at the same frequency with an amplitude that depends on the properties of the sample and the parameters of the device (see Methods). The motions of the magnet deform contacting tissues and induce associated strains in the metal traces of the sensor (Fig. 2a). Periodic variations of the resistances of these traces produce changes in V_S upon application of a constant current I_S. The magnitude of the strain, and therefore V_S, depends on the elastic modulus of the tissue. Finite element analysis (FEA) quantifies the mechanical coupling between the actuator, the sensor and the tissues. The distribution of equivalent strain across the sensor structure appears in Fig. 2a for the case of measurements (V_A of 5V at 50 Hz) on artificial skin substrates (PDMS, 1 cm thick) with elastic moduli of 10 kPa, 100 kPa and 600 kPa. This range is relevant to human skin and other related tissues. The normalized strain in the sensor structure increases by a factor of ~2 as the tissue modulus decreases from 600 kPa to 10 kPa, with a corresponding increase in V_S. Details for FEA simulation is in the Supplementary Information.

Results of Fig. 2b and Supplementary Fig. 9 summarize the dependence of the amplitude of the motion of the magnet on V_A and *f* during operation on a sample of artificial skin (PDMS, 3 mm thick, 200 kPa). Here, different weight ratios of crosslinker in PDMS samples yield various desired moduli for these substrates. Independent measurements of elastic modulus exploit a biosoft intender (Hysitron Biosoft Indenter, Bruker) under quasi-static conditions (Supplementary Fig. 10). A high-speed camera allows direct visualization of the motions of the magnet during operation (see details in Methods), as a means for measuring amplitudes as small as a few hundreds of micrometers. The amplitude increases with V_A, with values of ~300 μm at a V_A of 5 V at 50 Hz (Fig. 2b), and also depends on *f*, with a resonance at ~200 Hz (Supplementary Fig. 9), consistent with results in recent publications[26].

As the alternating current drives the actuators, the lock-in amplifier determines V_S (Supplementary Fig. S3) at the same frequency. According to previous reports[21], the viscoelastic effects of typical biological samples are negligible at the relatively low operating frequencies explored here (<1000 Hz), such that

measurements can be considered as quasi-static[24]. As such, V_S relates to the static modulus of elasticity, as per FEA results. Figs 2c and d present values of V_S for artificial skin samples with elastic moduli of 10, 100 and 500 kPa (3 mm thick), as a function of V_A and f. The value of V_S increases with V_A (from 1 to 5 V) and f (from 30 to 110 Hz), consistent with trends in the amplitudes of the motions of the magnet (Fig. 2b and Supplementary Fig. 9). Here, samples with high modulus lead to low strain, and therefore low V_S, in agreement with FEA results in Fig. 2a. An important engineering consideration is that the coil can create electromagnetic induction effects on the sensor during measurements, thus generating some cross-talk with V_S at high frequency (~10 μV at 1000 Hz with V_A of 5 V, see details in Supplementary Fig. 11). This consideration favors low frequency (<100 Hz) operation, where such inductive effects induce voltages that are approximately two orders of magnitude lower than those associated with the sensor signals. Unless otherwise stated, the following studies use a fixed f (*e.g.* 50 Hz) and V_A (5V).

Fig. 2e demonstrates that the value of V_S decreases with increasing modulus (10 kPa to 2 MPa) at various f (30, 50 and 70 Hz) for samples of artificial skin with thicknesses of 3 mm, each supported by a glass wafer (Supplementary Fig. 10) to simulate underlying bones. In the regime of low modulus, the actuator vibrates relatively freely, with correspondingly high levels of localized deformation, large strains and thus large V_S. For high modulus, the sample limits the deformations, thereby yielding small V_S. Samples with moduli less than 500 kPa (red in Fig. 2e) are of particular interest because they are most relevant to many soft biological tissues, also with high sensitivity to output V_S (Fig. 2f). The experimentally measured (symbols) and FEA-simulated (lines) V_S vary consistently with modulus from 10 kPa to 500 kPa. Here, increasing the thickness also increases V_S, mostly due to the decreasing effects of the rigid support (glass wafer) in limiting the deformations. Fig. 2g summarizes FEA and experimental results for the thickness dependence of V_S for different tissue moduli. Such thickness effects diminish as the thickness of the target increases to values larger than several millimeters, to define a saturation depth (7~8 mm) for the measurements, as demonstrated in Fig. 2g. As in Supplementary Fig. 12, the results reveal the dependence of V_S on tissue modulus for samples with thicknesses (2 cm) that exceed the saturation depth.

An analytical expression can be determined for the output voltage $V_S = f(E, H, \text{and } V_A)$ in the case of small deformations (Equation 1), by fitting the experimental and simulation data (Supplementary Fig. 13) as

$$V_s = \mathrm{C}(E) \cdot \tanh\left[\left(\frac{H}{H_0}\right)^{1/2}\right] \cdot V_A, \qquad (1)$$

where the V_S is linearly proportional to the input V_A (5 V in the current experiments) in this regime of small deformations, H is the thickness of the target tissue and H_0 is the saturation depth. $C(E)$ is a

dimensionless coefficient that depends on the elastic modulus (E) of the tissue, as in Supplementary Table 1 obtained from FEA results. For a given device design, the measured V_S and H, together with Equation 1 and Supplementary Table 1, provide a simple, yet accurate way to determine the modulus of the target tissue. The dimensionless coefficient C should only depend on the non-dimensional, normalized tissue modulus, such as the ratio of E to the effective modulus of the device.

Measurements on hydrogels, and on porcine and human skin. The EMM sensor can characterize the mechanical properties of a range of biomaterials and skin regions both *ex vivo* and *in vivo* (Figure 3). Recent research shows that hydrogels (poly(ethylene-glycol) diacrylate, Sigma-Aldrich) at different levels of hydration (water concentration) have Young's moduli that span those associated with most soft biological tissues in animal models and human subjects[28-30]. Fig. 3a presents results from samples with various levels of hydration, at thicknesses of ~4 mm (inset of Fig. 3a). V_S increases with hydration from 30 wt% to 80 wt%. The results in Fig. 2g yield corresponding values of elastic modulus, as in Fig. 3b (blue), that range from ~37 kPa to ~1.5 MPa, consistent with values (green in Fig. 3b) obtained using the biosoft indenter (Hysitron Biosoft Indenter, Bruker). Similarly, Fig. 3c shows results obtained with samples of abdominal porcine skin (2 mm thick; inset of Fig. 3c). Here, increasing the hydration level to 40 wt% yields V_S of ~34 μV. Comparisons are quantitatively consistent with measurements using the indenter for each hydration level, corresponding to a range from 95 kPa to ~1 MPa (Fig. 3d). Details on preparation steps and measurement results appear in Methods.

Capabilities extend to direct measurements of skin at various locations of the body of volunteer subjects, as illustrated in Fig. 3e. A collection of photographs illustrate applications across main regions (*e.g.* biceps, abdomen, thigh, forearm, *etc*). The measurement repeatability at a specific location represents an important metric. Results of multiple cycles of measurement from the forearm appear in Fig. 3f (*i.e.* 10 times). The average and standard deviation of V_S are 47.5 μV and 0.8 μV, respectively. The inset (Fig. 3f) shows that the noise decreases with the square root of averaging time for an individual measurement (*i.e.* integration time, t; the duration of a measurement operation that yields the value of V_S). As an example, increasing the integration time from 1 ms to 10 s decreases the noise from ~1 μV to ~10^{-2} μV, approximately two orders of magnitude smaller than the signal.

The measurements determine the average elastic modulus of the skin to a characteristic depth of ~8 mm, as previously demonstrated in Fig. 2g. Each location in Fig. 3e includes the skin, superficial fat, underlying muscle tissues, *etc*, with a total tissue thickness that exceeds this characteristic depth[31-33]. Measurements of elastic modulus at different locations on the body from ten healthy volunteer subjects with ages between 25-32 years and ten with ages between 60-68 years are in Fig. 3g (determination of modulus values rely on results in Supplementary Fig. 12). The results lie within expected values for human skin and *ex vivo* biomaterials determined in the small strain regime using techniques based on suction[11,12], torsion[13] and indentation[10]. The devices operate well on both hair bearing and hairless areas of the skin (Supplementary Fig. 14). Bending around curved surfaces induces only minor changes in the results (Supplementary Fig. 6). Consistent with expectation and recent reports[2], the moduli increase with

age, typically due to a loss in hydration[34], in accordance with Figs. 3b and d. Detailed information for these clinical tests appears in *SI Appendix*. The modulus can also depend on the tension in the skin due to non-linear mechanical responses associated with collagen and elastin fibers in the dermis[35]. The tension typically decreases with increasing age[2], thereby reducing the apparent modulus[36].

Muscle activity can also affect the moduli measured across depths associated with the devices reported here. An example in Fig. 3h shows a device on the forearm in a relaxed state and in a tensed condition due to lifting a dumbbell. Repetitive cycles of movements during real-time recordings of V_S yield moduli values that vary continuously between minimum and maximum values of 205 kPa and 320 kPa, respectively (details of dynamic measurements appear in Methods). These values correspond to average moduli of the skin and underlying muscles to a characteristic depth of ~8 mm. Recent studies based on ultrasound elastography methods[37] report muscle moduli that exhibit a similar trend (*e.g.* the modulus of biceps muscles increases by ~100 kPa due to contraction)[38,39]. Such capabilities may support various applications in kinesiology and rehabilitation.

Results obtained from patients with skin diseases in clinical settings appear in Figure 4. These measurements reveal localized variations in skin modulus associated with lesions. A tissue-phantom model (Supplementary Fig. 15) for this case combines a low modulus silicone substrate (8 mm thick, 5 cm diameter) as healthy skin (~100 kPa) with a local high modulus silicone insert in the center (1 cm diameter; ~500 kPa) as the lesion. Measurements of modulus in the central region and nearby surrounding parts yield expected results (Supplementary Fig. 16). Evaluations of five patients (ages: 28-37) with psoriasis distributed across various body regions (arm, hand and lower back) appear in Figs 4a, c and e. Details are in Methods. This condition leads to lesions in red patches of thick, scaly skin (over 1 cm diameter), and pathological changes in skin properties, such as thickness, stiffness and hydration[40,41]. An adhesive medical film (3M Tegaderm) placed over the structure and onto adjacent skin prevents relative motion during evaluations. The measurements yield modulus values for the lesions and for nearby regions of normal skin (Figs 4b, d and f) for each location (Supplementary Fig. 17). As expected, the lesions (black frames, Figure 4) exhibit higher moduli than those of nearby skin, due primarily to differences in skin elasticity and hydration[42]. These rapid (~1 min), simple measurements have potential clinical significance in rapidly identifying and targeting of skin lesions, with quantitative metrics that have promise as diagnostic biomarkers for a range of skin conditions.

Miniaturized designs for multilayer biological targets. In addition to measuring elastic modulus to relatively large depths (over 8 mm), the lateral dimensions of the devices can be reduced, in a manner guided by computational modeling, to reduce these depths to values approaching those of the dermis (~1 mm). As an example, Fig. 5a summarizes devices that have sensing areas (surface area of the magnet) with diameters (D) from 8 mm to 1.5 mm, all with magnets that have the same thickness (1.5 mm). Fig. 5b shows experimental (symbols) and simulated (lines) FEA results for V_S from devices with different D (3 mm and 1.4 mm) on a single, thick layer of artificial skin (PDMS, 2 cm thick) as a function of elastic modulus. Here, reducing D decreases the contacting area between the device and sensor, and therefore

lead to decreases in V_S for a given f (50 Hz) and V_A (5 V). Fig. 5c shows the cross-sectional strain distributions obtained by FEA in a sufficiently thick tissue with elastic modulus of 200 kPa, subjected to pressure on the surface from devices with different D. The distributions exhibit saturation depths (red lines in Fig. 5c) that decrease with D (*i.e.* ~8.2 mm for D= 8 mm, ~3.3 mm for D= 3 mm and ~1.6 mm for D= 1.5 mm), consistent with experimental results (Fig. 2g and Supplementary Fig. 18). The results suggest the basis for depth profiling of the modulus, of relevance for many types of biological tissues. For skin, the stratum corneum, epidermis and upper dermis (typically 1~2 mm thick) serve as protective barriers against environmental hazards for subcutaneous tissues that consist of superficial fat and connective muscles over bones. These layers exhibit different moduli and thicknesses. Fig. 5d presents a bilayer architecture of silicone materials that approximates the structure of skin/tissue, fabricated with different thicknesses (h_A = 1.8 mm; h_B >> 1 cm) and different moduli (E_A = 200 kPa; E_B = 50 kPa). Measurements using devices with different D can determine the equivalent mechanical properties of this bilayer structure. Here, V_S is 30 μV and 20 μV for devices with D of 3 mm and 1.5 mm, respectively. These V_S depend on both (1) sensing area (D), and (2) the modulus of each layer. Fig. 5e shows the results of FEA simulation of V_S for layer moduli in the ranges of E_A = 100~300 kPa and E_B = 10~100 kPa, with different EMM sensors (D of 3 mm and 1.5 mm). For V_S = 30 μV and D = 3 mm, the simulated relationship between E_A and E_B, marked with the red curve, appears in the left of Fig. 5e. Similarly, for V_S = 20 μV and D = 1.5 mm, the relationship between E_A and E_B marked with the black curve, appears in the right of Fig. 5e. The intersection of these two curves thus determines the calculated modulus for each layer, as 198 kPa and 52 kPa for E_A and E_B (Fig. 5f), respectively, which are in excellent agreement (within 5 % error) with the moduli of the sample in Fig. 5d.

To showcase this multilayer capability in clinical practice, Fig. 5g summarizes the results of moduli measured on the cheek areas and fingertip joint (near the nail plate) in human subjects (details appear in Supplementary Fig. 19). As an example of the former, literature reports indicate that the combined thickness of the epidermis and dermis is ~1.8 mm in the cheek region[43], and that other tissues (*i.e.* superficial fat and muscle) appear beneath the dermis. Measurements using devices with D of 3 mm and of 1.5 mm yield V_S of 28.7 μV and 19.3 μV on cheek, respectively. By utilizing the simulation curves of V_S for both cases from Fig. 5e and locating the intersection point as in Supplementary Fig. 19a, the cheek moduli are (1) 248 kPa for the skin layer with thickness of 1.8 mm; and (2) 59 kPa for inner tissues (blue in Fig. 5g). These measured moduli are consistent with values reported for the cheek region[44] and associated superficial fat in human subjects[45].

In addition to body areas such as the cheek with comparatively large tissue thicknesses, measurements on regions where bones lie near the surface (*e.g.* hand joints, fingertip dorsum, *etc*), where the tissue structure is thin, are of particular interest in clinical diagnosis and treatment of dermal pathologies such as scleroderma[5]. As an example, consider a simple estimate of the combined thickness of skin and tissues (~3 mm; ~2 mm for the skin and ~1 mm for the underlying tissues) in the fingertip joint near the nail plate for a volunteer subject (Supplementary Fig. 20)[46,47]. Measurements with EMM sensors yield V_S

of 27.1 μV (D = 3 mm) and 18.2 μV (D = 1.5 mm), corresponding to modulus values of (1) 316 kPa for the skin layer, and (2) 67 kPa for inner tissues at this region of the body (red in Figure 5G and Supplementary Fig. 19b). These results agree with those determined using conventional approaches[45,48]. These findings demonstrate that a combined set of EMM sensors with appropriate D allow modulus characterization for multilayer biological targets with different thicknesses, across a wide range that involves not only bulk geometries (deep tissue scale) but also near-surface regions (superficial depth).

Interconnected arrays of devices for spatial mapping of modulus. Multiple EMM sensors can be used separately, as described above, or they can be configured into arrays, as show in Figure 6. Here, Fig. 6a presents a photograph of a collection of strain sensors printed onto a polymer substrate before interconnection (fabrication procedures appear in Methods), highlighting mechanical flexibility (Supplementary Fig. 21) for wrapping areas of interest across the body, as shown on the back in Fig. 6b (volunteer subject, age of 32, male). Fig. 6c presents a schematic illustration of a 4 × 4 array of this type (4 columns, 4 rows, area of ~100 cm^2, thickness of system as ~2.5 mm) after assembly of vibratory actuators (Supplementary Fig. 22). Fig. 6d summarizes an equivalent circuit diagram of the system. Interconnection to multiplexers allows rapid readout of signals from each unit cell in a time sequence controlled by a data acquisition (DAQ) system that features a minimal number of addressing wires, with capabilities for defining the frequencies and amplitudes of input voltages to each EMM sensor via a function generator (Tektronix) as a power supply (Supplementary Fig. 23). Details appear in Methods.

The resulting multiplexed system can perform fast mapping of elastic modulus on curved, soft surfaces of tissues under quasi-static conditions. As an example, Fig. 6e shows results from measurements of elastic modulus across the back (Fig. 6b) during relaxed (left) and tensed states (right) associated with muscle contraction. Here, the actuator array (50 Hz; 5 V, Sine-wave) produces signals from the underlying sensor array. Each unit cell corresponds to an elastic modulus value determined from an individual EMM sensor with a corresponding spatial resolution of ~1.5 cm^2. Stretching the trapezius muscle (red frame in Fig. 6e) of the back in the tensed condition (right of Fig. 6e) leads to spatial variations of increased modulus associated with activation of this targeted muscle group. Specifically, the average modulus for the tensed condition corresponds to ~430 kPa, compared to ~310 kPa for relaxed state, consistent with expectation and recent literature[49].

Outlook

In summary, the results reported here establish the materials, device designs and integration schemes for a bio-integrated electromechanical system that can perform accurate, mechanical characterization of biological tissues in a non-invasive, rapid fashion. Detailed experimental and simulated investigations highlight the various features of device operation with a wide range of soft biomaterials and multilayer samples, and at various locations across human body under different conditions. Careful selection of device designs and integration of arrays of sensors support evaluations of depth dependent properties and spatial mapping, respectively. The findings presented here have potential as the basis for routine monitoring of variations in elastic modulus for diagnosis and treatment of various disease states,

applicable to nearly all parts of human body. Particularly promising opportunities are dermatology, where the data produced by these devices can assist in diagnosis, treatment tracking, and disease monitoring of medical dermatology, with natural extensions into aspects of aesthetic dermatology and recovery from surface wounds. Additional possibilities are in evaluating mechanical properties of the skin in a variety of physical conditions with an emphasis on age dependence[2] and the relationship between biomechanics and functionality[34]. The results may serve as predictors of potential for reactions of the skin to ageing, hydration loss and associated disorders, and further establish the role of skin in defining health status.

Methods

Fabrication of Sheets of Strain Sensors. As shown in Supplementary Fig. 1, the fabrication began with the formation of isolated strain sensors on a 4-inch silicon wafer (100 mm diameter, 500 μm thick, University Wafer) or a glass wafer (1 mm thick, VWR Vistavision LLC). After cleaning the substrate surface via RCA processes, a thin, spin-cast film of poly(methyl methacrylate) (PMMA, ~ 500 nm thick, MicroChem) served as the sacrificial layer on the substrate, and a support for a spin-cast a layer of polyimide (PI-2545, 1 μm thick, HD MicroSystems). Electron-beam evaporation of Cr/Au (5/100 nm) and photolithographically patterning defined the electrical traces and sensing regions. The serpentine patterns of the traces improved the fabrication yields. A second layer of polyimide (1 μm thick) encapsulated these features. Photolithography and reactive ion etching (RIE) with O_2 isolated the devices into a open-mesh structure (Supplementary Fig. 2). Subsequent processing released the sensor array from the handle wafer by immersion into acetone for 18 h to remove the sacrificial layer of PMMA. Transfer printing via a water soluble tape (Grainger), followed by deposition of adhesive layers (Ti/SiO_2, electron-beam evaporation, 5/50 nm thick), allowed delivery of selected sets of devices from this array onto a foreign substrate coated with thin layers of PDMS (~ 30 μm, Sylgard 184, Dow Corning). Here, ultraviolet ozone (UVO) treatment of the surfaces of devices and the top surfaces of the PDMS enabled strong bonding upon contact. Peeling the material stack from the temporary substrate yielded a piece of flexible electronics as the basis for the strain sensors, with excellent mechanical properties (Supplementary Fig. 5a). Fabrication of multiple sensors and repetitive transfer-printing onto a large-area layer of PDMS formed an array of such devices (Fig. 6a). Subsequent external wire connections relied on flexible cables and heat seal connectors (HSCs, Elform Inc.) to printed circuit boards (PCBs) for measurements, as shown Supplementary Fig. 3.

Assembly with Vibratory Actuators. Assembly of the vibratory actuators onto these sensors completed the integration, to yield components with capabilities in measuring the elastic modulus. Procedures for assembly of the vibratory actuator exploited schemes described elsewhere[26]. Briefly, the first step involved immersing a Cu coil (wire diameter of 50 μm, 240 turns, with an inter diameter of the coil of 2 mm and an outer diameter of 12 mm) into a layer of PDMS (diameter of 18 mm, 200 μm thick; 10:1 weight ratio of crosslinker) with the ends of the wire exposed to allow for external connection. The structure was then cured at 70 ^oC overnight. Next, the ring-shaped PDMS shell was cut into suitable size (inter and outer diameter of 12 mm and 18 mm, 2.4 mm thick) and then bonded onto the coil/PDMS

structure via a commercial adhesive (Kwik-Sil, World Precision Instruments). In parallel, a nickel-coated neodymium magnet (8 mm diameter, 1.5 mm thick) mounted on the center of a polyimide disk (18 mm diameter, 75 μm thick) with a strong dual-side adhesive (Kapton, DuPont). Carefully aligning the coil/PDMS ring and magnet/polyimide disk yielded a vibratory actuator, bonded together with a silicone adhesive applied on the contacting area (Kwik-Sil, World Precision Instruments). The final step involved deposition of a layer of SiO_2 (electron-beam evaporation, 100 nm thick) on the bottom surface of a polyimide disk across only a ring-shaped area (Fig. 1a). UVO treatment of the bottom surfaces of the actuator (polyimide-disk side) and the top surfaces of the fabricated sensor led to a strong bonding interface upon contact, to complete the assembly of the actuator and sensor. In this manner, the magnet of the actuator can vibrate in an out-of-plane direction in the ring-shaped PDMS shell, yielding pressure on the contacting tissue. Here, suction effects can be neglected due to the absence of a bonding interface between the sensing area of polyimide disk and strain sensor. The resulting overall system can directly laminate onto curved surfaces in an intimate contact, with stable measurements, as shown in Supplementary Fig. 6.

Measurement setup and operational principles. The measurement setup included two areas of focus: the actuation and the sensor, as shown in the schematic illustration of Supplementary Fig. 3. For quasi-static measurements, an output channel from a lock-in ampliefier (SRS SR830, Stanford Research) connected to the coil of EMM sensor to deliver a sine-wave voltage (V_A, ± 5 V) with well defined frequency and amplitude. The resultant current through the coil generated magnetic fields and associated time-dependent Lorentz forces to drive actuation and vibration of the magnet mounted on the thin polyimide disk. The result yielded a mechanism for imparting pressure onto the contacting tissues (Supplementary Fig. 7). The associated deformation of these tissues yielded strains distributed over the metal traces of the sensor. These responses allowed determination of the elastic modulus of the tissue. A constant current delivered from a current source (Keithley 6221, Tektronix) to the strain sensor (I_S) provided an input channel to the lock-in amplifier, to capture the amplitudes of periodic variations in the resistance of the strain sensor, as a sensing voltage (V_S) at the frequency of the vibration. Similarly, for dynamic measurements, a DAQ system (National Instrument, Inc.) interfaced by wired connections to the sensor captured dynamic recordings of V_S at a sampling frequency of 5 Hz during actuation of the system.

Procedures for bending tests and soak tests. EMM sensors can establish gentle interfaces to soft, curved biological tissues, with capabilities for stable electrical performance during immersion in biofluids. Bending tests appear in Supplementary Fig. 6a, where the systems intimately couple onto cylindrical substrates of artificial skin layer (PDMS, 200 kPa) with different curvatures, all with characteristic depth over 8 mm at the contacting location. At bending radii ranging from 4 cm to ∞, the value of V_S remained unchanged (Supplementary Fig. 6b), due to the neutral mechanical plane at the tissue interface.

Soak tests involved electrical measurements of devices during immersion in artificial sweat solution (pH of 4.5, Pickering laboratories) at elevated temperatures (50 ^{O}C). During the tests, the sensors, consisting of a trilayer structure of polyimide / metal traces / polyimide (1 μm/100 nm/1 μm thick), mounted on a

thin layer of PDMS with a weight ratio of crosslinker of 40:1. A thin, waterproof layer of Tagederm film (3 M) encapsulated the front side the device, as shown in Supplementary Fig. 5b. Measurements demonstrated stable electrical performance during 7-day immersion.

Preparation of artificial skin samples. Drop casting thick layers of PDMS with various thicknesses in a glass petri-dish formed artificial skin samples for purposes of validating the device operation (Supplementary Fig. 10a). These PDMS samples (area of 5×5 mm^2) involved different weight ratios of crosslinker to base, ranging from 3:1 to 60:1, all cured at room temperature over a day. As described in previous publications, the resulting artificial skins exhibit a range of elastic moduli. Viscoelastic effects can be neglected during measurements with actuation frequencies less than 100 Hz[20]. The effects of inertia are negligible because of the low frequencies, such that the measurements on these artificial skin samples and biomaterials can be considered as quasi-static[21].

Measurement of elastic modulus using in-situ **bio-indenter.** An *in-situ* bio-indenter (Hysitron Biosoft Indenter, Bruker) allowed quantitative analysis of the elastic modulus for each sample used for this work, including hydrogel, porcine skin, and PDMS artificial skins. The measurement relied on a 20 μm-diameter spherical probe to indent into the surface of a test sample, where the loading force as a function of the probe displacement was recorded continuously (Normal bit force resolution, ~ 1 nN). The Hertz model can fit the elastic regime of the collected data, to yield the final elastic modulus. As an example, measurement results for a set of PDMS artificial skin samples (dimension as 5 mm × 5 mm × 1 cm, width × length × thickness) appear in Supplementary Fig. 10b, as a function of weight ratios of crosslinker. For instance, PDMS samples with weight ratio of crosslinker to base as 15:1 correspond to a measured elastic modulus of ~ 500 kPa.

Visualization of actuator operation. The vibratory amplitude represents a key parameter for device operation during mechanical measurements. A high-speed, high-resolution camera can simply capture a video in slow motion to allow for direct visualization of the actuators, including the amplitudes and orientations of the vibratory motions, as shown in the Supplementary Movie 1. Similar procedures are used in other recently reported studies[26]. The results of vibratory amplitudes show relationships with frequencies of f and input voltages of V_A.

Electromagnetic induction effect. During the measurement, alternating currents through the top coil of the actuator can induce an electromagnetic induction effect associated with the metal traces that define the strain sensor and the flower-shape mesh structure, thereby resulting in additional output voltage. To facilitate measurement of this induction effect, the magnet was removed from actuator during V_A input into the top coil. As shown in Supplementary Fig. 11, the induced output voltages were separately measured as a function of actuation frequencies (10–10,000 Hz), while the EMM sensor without the magnet couples onto a sample of artificial skin with elastic modulus of 200 kPa. The induced voltages remained below ~ 0.5 μV at low frequency (below 100 Hz), which were ~ 2 orders of magnitude lower than the signals. This effect increased with increasing actuation frequency, with an output voltage higher than 10 μV at 1000 Hz.

Preparation for hydrogel samples and porcine skins with different hydration levels. Validation studies involved measurements of hydrogels and abdominal skin from porcine models, both with different hydration levels. For the hydrogel, a set of samples were synthesized by mixing different amounts (wt %) of poly(ethylene-glycol) diacrylate (Sigma-Aldrich) and de-ionized water. Powders of methylpropiophenone (2-Hydroxy-4'-(2-Hydroxyethoxy)-2-methylpropiophenone, ~ 0.6 wt %, Sigma-Aldrich) served as the initiator in the solution mixture, followed by UVO treatment for rapid curing in a mold of petri dish (area of 25 cm^2, 4 mm thick), with different elastic moduli for each hydration level. For the porcine skin, fresh samples from the abdominal region were cut (3 × 4 cm^2, 2 mm thick) and baked at 50 ^oC in an oven for over 48 hours to evaporate the water content inside. The resulting weight of W_0 defined a hydration level of 0. Subsequently, submerging the samples into Dulbecco's phosphate-buffered saline (DPBS) solution at 37 ^oC for sufficiently long periods (~ 1 day) yielded fully saturated samples, corresponding to a maximum hydration state, with a weight of W and a hydration level that can be calculated as the percentage $(W - W_0)/W$. Similarly, different timescales for immersion in DPBS solution yielded samples with different hydration levels. A bio-indenter was used to evaluate the elastic modulus of these samples.

Information for Clinical Tests and Simulated Evaluation. All subject participation was fully voluntary and submitted the informed consent prior to tests. The research protocol was approved by Northwestern University's Institutional Review Board and the Northwestern Memorial Hospital (Protocol Number: STU00206331-CR003) and registered on ClinicalTrials.gov (Registration Number: NCT03461549). Twenty volunteers (ten young: 25–32 years old; ten old: 60–68 years old) were recruited for studies on normal healthy skin without skin lesions, as in Fig. 3g. Five patients with skin disorders such as plaque psoriasis were involved in clinical tests, as demonstrated in Supplementary Fig. 17. The pathological symptom included red, thick patches of skin lesion (typically over 8 mm diameter) with low hydration level across skin surface, and can be detected through physical palpations with detectable differences in skin properties such as stiffness and thickness. All of these volunteers and patients were at rest during the measurements.

After a process of cleaning pre-selected skin areas (lesion and normal) by gentle rubbing with alcohol wipes, the EMM sensors were mounted onto the relevant skin areas followed by conformal coverage with a medical dressing (Tegaderm, 3M) to secure device placement. The placement of the sensors was performed by research staff and/or medical doctors. The EMM sensors were pre-connected to a DAQ system (including a locking-in amplifier and a current source) located within the operational room. Data recording began after 10 s of system warm-up, to ensure stable operation. Each subject performed 1-min measurement in a resting position. Data were collected and stored for further data analysis on a tablet computer. Similar to the operation on patients, a corresponding measurement that simulated clinical tests on a tissue-phantom model appears in Supplementary Fig. 15.

Operation for Multiplexed Arrays of EMM Sensors. Fabrication of multiple strain sensors and repetitive transfer-printing onto a large-area layer of PDMS form an array of sensors (Supplementary Fig. 21) and

electronic interconnects based on flexible, lightweight conductive cables (heat seal connectors (HSCs), Elform Inc.). Connection to an external multiplexing board allow for an interface to a 4:1 multiplexer that enables readout from each sensor at a time, as controlled via a back-end DAQ system. Assemblies of actuators aligned with the strain sensor array yielded the complete mapping systems (Supplementary Fig. 22).

Operation of the multiplexed array of EMM sensors appears in Supplementary Fig. 23. During measurements, all of the actuators are connected for vibration at a specific frequency (f) and amplitude of input voltage. The setup for spatial mapping of the skin modulus used a function generator (Tektronix) to produce a sine-wave power input with preprogrammed frequency and amplitude, delivered through the interface board to certain actuators in the mapping system. For the strain sensor array, a current source connected through the interface board to a multiplexer delivered current to a certain sensor in the system. A lock-in amplifier (SRS SR830, Stanford Research) connected through the interface board to a demultiplexer captured the corresponding change in voltage, to yield the elastic modulus and/or hydration level at the corresponding location. Here, the multiplexers modulated by the controller enabled continuous scanning of the arrays of the EMM sensors at a sampling rate 5 Hz. With a constant current delivered from the current source (Keithley 6221, Tektronix) to the strain sensor, the lock-in amplifier (SRS SR830, Stanford Research) captured the amplitude of fluctuations in the resistance of the strain sensor by measuring the sensing voltage at certain frequencies.

Declarations

Acknowledgements

This work was supported by the Querrey/Simpson Institute for Bioelectronics at Northwestern University. We acknowledge the use of facilities in the Micro and Nanotechnology Laboratory for device fabrication and the Frederick Seitz Materials Research Laboratory for Advanced Science and Technology for device measurement at the University of Illinois at Urbana–Champaign. Z.X. acknowledges the support from the National Natural Science Foundation of China (Grant No. 12072057) and Fundamental Research Funds for the Central Universities (Grant No. DUT20RC(3)032). Y.H. acknowledges the support from NSF (CMMI1635443).

Author contributions

E.S., Z.X., W.B., X.Y., Y.H. and J.A.R. designed the research; E.S., Z.X., W.B., H.L., X.N., Y. X., J.M.B., Y.L., X.S., H.-Y.C., J.H.K., S.M., S.M.W., X.Z., D.J.M., M.H., S.X., X.Y., Y.H. and J.A.R. performed the research; E.S., Z.X., W.B., B.J., R.A., K.Y., Y.M., X.G., X.Y., Y.H. and J.A.R. analyzed data; E.S., Z.X., B.J., R.A., X.G., Y.H. and J.A.R. performed structural designs and mechanical modeling; and E.S., Z.X., W.B., X.Y., Y.H. and J.A.R. wrote the paper.

Competing interests

The authors declare no competing interests.

References

1. Joodaki, H. & Panzer, M. B. Skin mechanical properties and modeling: a review. *Proc. IMechE Part H: J. Engineering in Medicine* **00**, 1-21 (2018).
2. Pawlaczyk, M., Lelonkiewicz, M. & Wieczorowski, M. Age-dependent biomechanical properties of the skin. *Postepy Dermatol. Alergol* **5**, 302-306 (2013).
3. Pandya, H. J., Chen, W., Goodell, L. A., Foran, D. J. & Desai, J. P. Mechanical phenotyping of breast cancer using MEMS: a method to demarcate benign and cancerous breast tissues. *Lab Chip* **14** , 4523–4532 (2014).
4. Leblanc, N. et al. Durometer measurements of skin induration in venous disease. *Dermatol. Surg.* **23**, 285-287 (1997).
5. Khanna, D. et al. Standardization of the modified Rodnan skin score for use in clinical trials of systemic sclerosis. *J. Scleroderma Relat. Disord.* **2**, 11–18 (2017).
6. Batisse, D., Bazin, R. & Baldeweck, T. Influence of age on the wrinkling capacities of skin. *Skin Res. Technol*. **8**, 148-154 (2002).
7. Diridollou, S. et al. Sex and site dependent variations in thickness and mechanical properties of human skin in vivo. *Int. J. Cosmet. Sci.* **22**, 421-435 (2000).
8. Kashibuchi, N., Hirai, Y., O'Goshi, K. & Tagami, H. Three-dimensional analyses of individual corneocytes with atomic force microscope: Morphological changes related to age, location and to the pathologic skin conditions. *Skin Res. Technol.* **8**, 203-211 (2002).
9. Lulevich, V., Zink, T., Chen, H-Y., Liu, F-T. & Liu, G. Cell mechanics using atomic force microscopy-based single-cell compression. *Langmuir* **22**, 8151-8155 (2006).
10. Zheng, Y. and Mak A. F. T. Effective elastic properties for lower limb soft tissues from manual indentation experiment. *IEEE Eng. Med. Biol. Soc.* **7**, 257-267 (1999).
11. Diridollou, S. et al. *In vivo* model of the mechanical properties of the human skin under suction. *Skin Res. Technol.* **6**, 214-221 (2000).
12. Hendriks, F. M. et al. A numerical-experimental method to characterize the non-linear mechanical behaviour of human skin. *Skin Res. Technol.* **9**, 274-283 (2003).
13. Agache, P. G., Monneur, C., Leveque, J. L. & Rigal, J. D. Mechanical properties and Young's modulus of human skin *in vivo*. *Arch. Dermatol. Res.* **269**, 221-232 (1980).
14. Fischer-Cripps, A. C. Critical review of analysis and interpretation of nanoindentation test data. *Surf. Coat. Technol.* **200**, 4153-4165 (2006).
15. Gennisson, J. L. et al. Assessment of elastic parameters of human skin using dynamic elastography. *IEEE Trans. Ultrason. Ferroelectr. Freq. Control* **51**, 980-989 (2004).
16. Castera, L., Vilgrain, V. & Angulo, P. Noninvasive evaluation of NAFLD. *Nat. Rev. Gastroenterol. Hepatol.* **10**, 666–675 (2013).

17. Manduca, A. et al. Magnetic resonance elastography: Non-invasive mapping of tissueelasticity. *Medical Image Analysis* **5**, 237–254 (2001).
18. Huang, C.-T., Shen, C.-L., Tang, C.-F. & Chang, S.-H. A wearable yarn-based piezo-resistive sensor. *Sens. Actuators A* **141**, 396–403 (2008).
19. Rogers, J. A., Someya, T. & Huang, Y. Materials and mechanics for stretchable electronics. *Science* **327**, 1603–1607 (2010).
20. Dagdeviren, C. et al. Conformal piezoelectric systems for clinical and experimental characterization of soft tissue biomechanics. *Nat. Mater.* **14**, 728–736 (2015).
21. Yu, X. et al. Needle-shaped ultrathin piezoelectric microsystem for guided tissue targeting via mechanical sensing. *Nat. Biomed. Eng.* **2**, 165-172 (2018).
22. Han, S. et al. Battery-free, wireless sensors for full-body pressure and temperature mapping. *Sci. Transl. Med.* **10**, eaan4950 (2018).
23. Lipomi, D. J., et al. Skin-like pressure and strain sensors based on transparent elastic films of carbon nanotubes. *Nat Nanotechnol* 6:788–792 (2011).
24. Son, D, et al. Multifunctional wearable devices for diagnosis and therapy of movement disorders. *Nat Nanotechnol* 9:397–404 (2014).
25. Yeh, W.-C. et al. Elastic modulus measurements of human liver and correlation with pathology. *Ultrasound Med. Biol.* **28**, 467–474 (2002).
26. Yu, X. et al. Skin-integrated wireless haptic interfaces for virtual and augmented reality. *Nature* **575**, 473-479 (2019).
27. I. R. Minev, et al. Electronic dura mater for long-term multimodal neural interfaces. *Science* **347**, 159 (2015).
28. Wang, L. et al. Ultrasoft and highly stretchable hydrogel optical fibers for *in vivo* optogenetic modulations. *Adv. Optical Mater.* 1800427 (2018).
29. J. Y. Sun, et al. Highly stretchable and tough hydrogels. *Nature* **489**, 133-136 (2012).
30. J. J. Guo, et al. Highly stretchable, strain sensing hydrogel optical fibers. *Adv. Mater.* **28**, 10244 (2016).
31. Akkus, O., Oguz, A., Uzunlulu M., Kizilgul, M. Evaluation of skin and subcutaneous adipose tissue thickness for optimal insulin injection. *J. Diabetes Metab.* **3**, 1000216 (2012).
32. Kiliaridis, S. & Kälebo, P. Masseter muscle thickness measured by ultrasonography and its relation to facial morphology. *J. Dent. Res.* **70**, 1262-1265 (1991).
33. Jain, S. M., Pandey, K., Lahoti A. & Rao P. K. Evaluation of skin and subcutaneous tissue thickness at insulin injection sites in Indian, insulin naïve, type-2 diabetic adult population. *Indian J. Endocrinol. Metab.* **17**, 864-870 (2013).
34. Pedersen, L. & Jemec, G. B. E. Mechanical properties and barrier function of the skin. *Acta. Derm. Venereol.* **86**, 308–311 (2006).

35. Laiacona, D. et al. Non-invasive in vivo quantification of human skin tension lines. *Acta Biomaterialia* **88**,141–148 (2019).
36. Jacquet, E., Josse, G., Khatyr, F. & Garcin, C. A new experimental method for measuring skin's natural tension. *Skin Res. Technol.* **14**, 1-7 (2008).
37. Nordez, A. & Hug, F. Muscle shear elastic modulus measured using supersonic shear imaging is highly related to muscle activity level. *J. Appl. Physiol.* **108**, 1389–1394 (2010).
38. Yoshitake, Y., Takai, Y., Kanehisa, H. & Shinohara, M. Muscle shear modulus measured with ultrasound shear-wave elastography across a wide range of contraction intensity. *Muscle & Nerve* **50**, 103-113 (2014).
39. Shinohara, M., Sabra, K., Gennisson, J., Fink, M. & Tanter, M. Real-time visualization of muscle stiffness distribution with ultrasound shear wave imaging during muscle contraction. *Muscle & Nerve* **42**, 438-441 (2010).
40. Lewis-Beck, C., Abouzaid, S., Xie, L., Baser, O. & Kim, E. Analysis of the relationship between psoriasis symptom severity and quality of life, work productivity, and activity impairment among patients with moderate-to-severe psoriasis using structural equation modeling. *Patient Prefer Adherence* **7**, 199-205 (2013).
41. Kim, S. D., Huh, C. H., Seo, K. I., Suh, D. H. & Youn, J. I. Evaluation of skin surface hydration in Korean psoriasis patients: a possible factor influencing psoriasis. *Clin. Exp. Dermatol.* **27**, 147-152 (2002).
42. Dobrev, H. *In vivo* study of skin mechanical properties in psoriasis vulgaris. *Acta. Derm. Venereol.* **80**, 263-266 (2000).
43. Kim, T.-S. et al. Regional thickness of facial skin and superficial fat: application to the minimally invasive procedures. *Clin. Anat.* **32**, 1008-1018 (2019).
44. Kalra, A., Lowe, A. & Al-Jumaily A. M. Mechanical behaviour of skin: a review. *J. Material Sci. Eng.* **5**, 1000254 (2016).
45. Li, C., Guan, G., Reif, R., Huang, Z. & Wang R. K. Determining elastic properties of skin by measuring surface waves from an impulse mechanical stimulus using phase-sensitive optical coherence tomography. *J. R. Soc. Interface* **9**, 831–841 (2012).
46. Pejovi-Mili, A., Brito, J. A., Gyorffy, J. & Chettle, D. R. Ultrasound measurements of overlying soft tissue thickness at four skeletal sites suitable for in vivo x-ray fluorescence. *Med. Phys.* **29**, 2687-2691 (2002).
47. Fredriksson, I., Larsson, M. & Strömberg, T. Optical microcirculatory skin model: assessed by Monte Carlo simulations paired with *in vivo* laser Doppler flowmetry. *J. Biomed. Opt.* **13**, 014015 (2008).
48. Wiertlewski, M. & Hayward, V. Mechanical behavior of the fingertip in the range of frequencies and Displacements relevant to touch. *J. of Biomechanics* **45**, 1869-1874 (2012).
49. Annaidh, A. N., Bruyère, K., Destrade, M., Gilchrist, M. D. & Otténio, M. Characterization of the anisotropic mechanical properties ofexcised human skin. *J. Mech. Behav. Biomed.* **5**, 139-148 (2012).

Figures

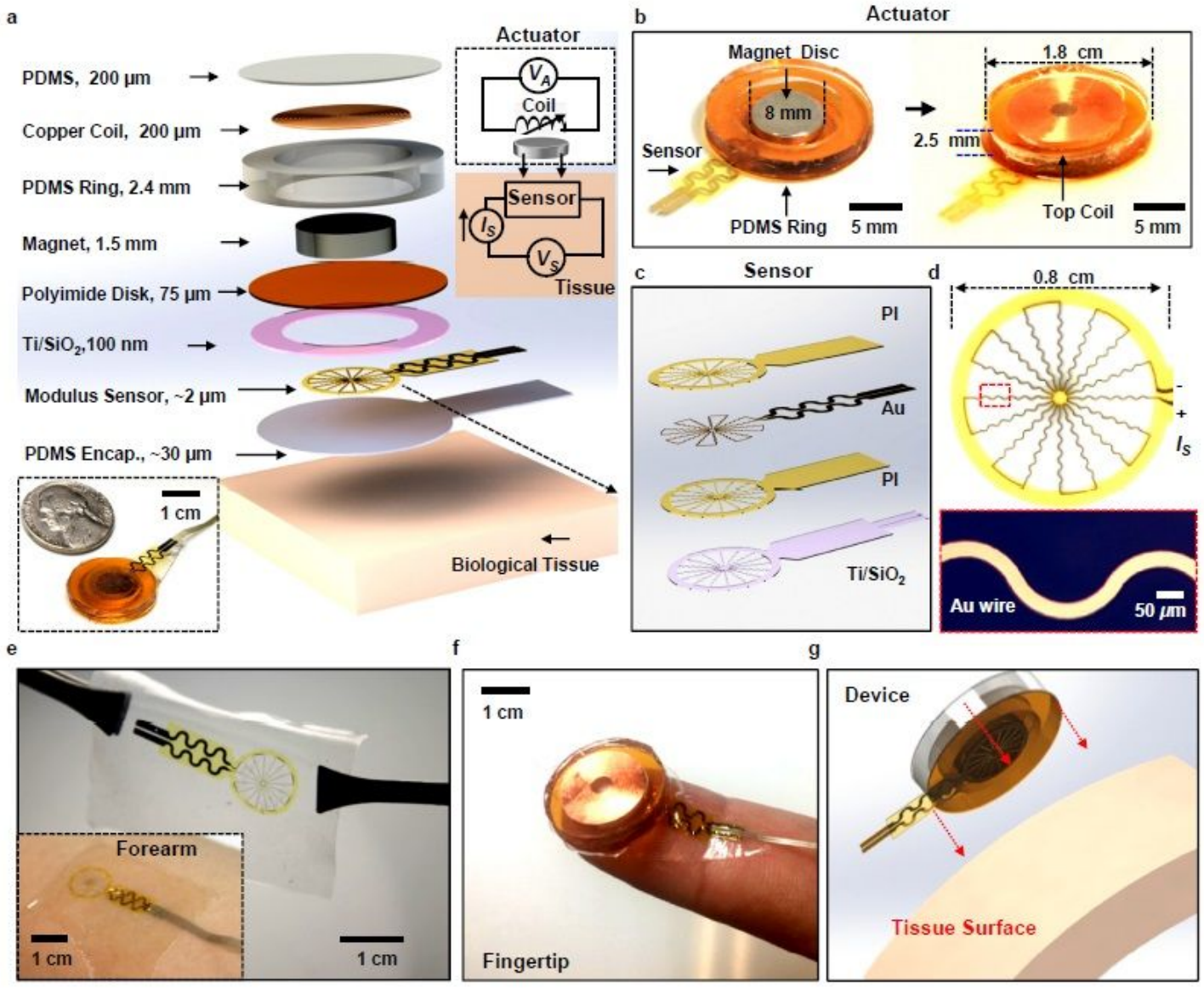

Figure 1

Millimeter scale electromechanical systems for sensing of soft tissue elastic moduli. (a) Exploded-view schematic illustration of the system. Upper inset shows a circuit diagram (upper-right) with an input voltage for the actuator (VA) and a sensing voltage from the sensor (Vs). Lower inset is a photograph of the back side of the system, next to a US nickel coin. (b) Photographs of the key constituent components of the system, including a copper coil (left) and a disc magnet (right). (c) Magnified view of the layer configuration of the sensor. (d) Schematic diagram of the sensor. (e) Photograph of the sensor. Inset is an image of the sensor laminated onto the skin of the forearm. (f) Photograph of the device on the fingertip. (g) Schemes for coupling the system onto the surface of human skin.

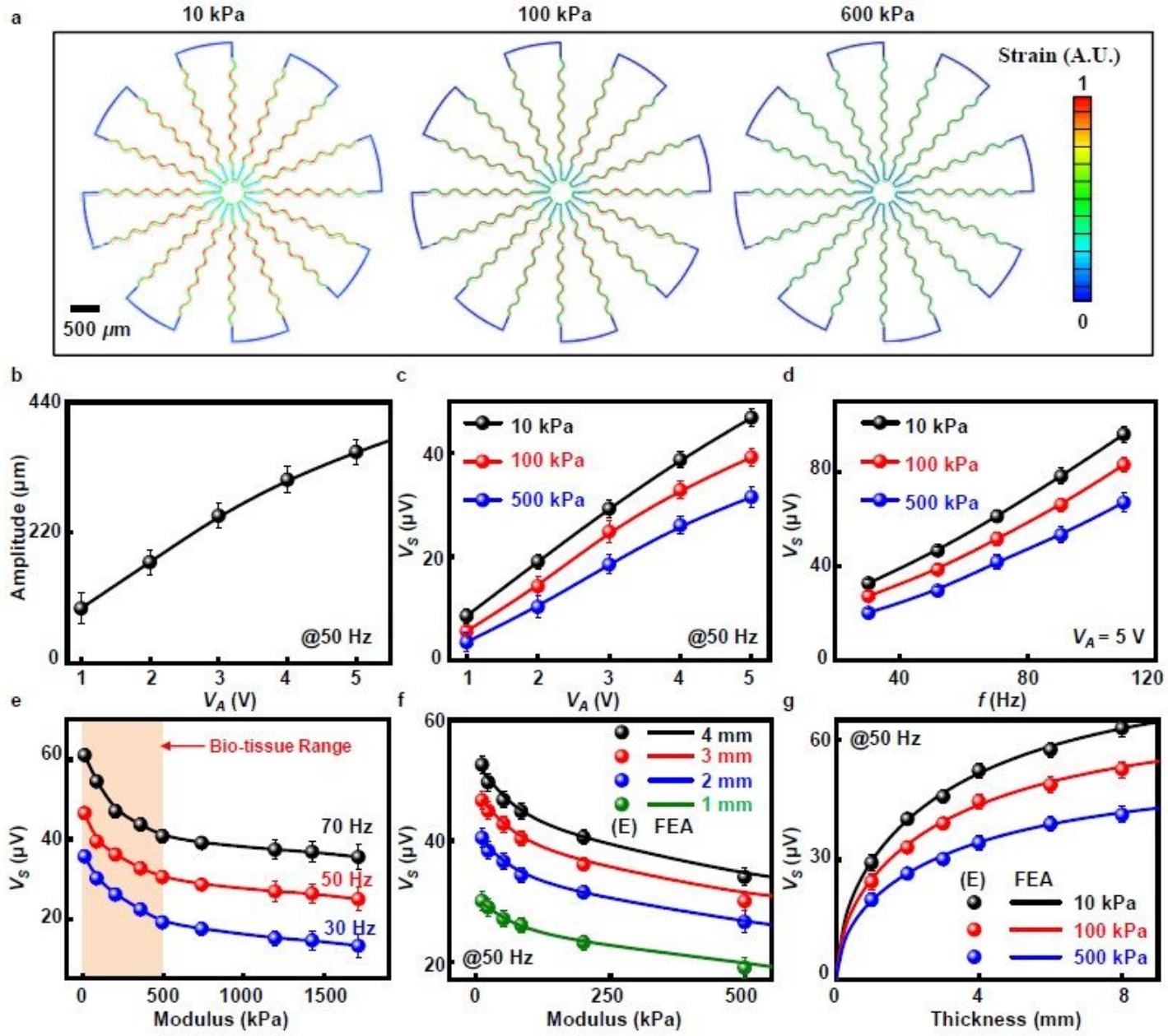

Figure 2

Experimental and simulation results on the device operation. (a) Finite element analysis (FEA) simulation results for the distribution of maximum strain across the sensor on artificial skin samples with elastic moduli of 10 kPa, 100 kPa and 600 kPa. (b) Vibrational amplitude of the magnet as a function of the amplitude of sine-wave input voltage (VA) while in contact with an artificial skin sample with a modulus of 200 kPa. (c), (d) Vs as function of (c) VA and (d) actuation frequency. (e) VS as a function of modulus at various frequencies. Error bars correspond to the standard deviation for at least 10 measurements with a given device. (f) Experimental (E, symbols) and simulation (FEA, line) results of VS as a function of sample modulus with various sample thicknesses. (g) Vs as function of thicknesses of samples with various moduli. The symbols and lines correspond to experimental (E) and simulation (FEA) results, respectively.

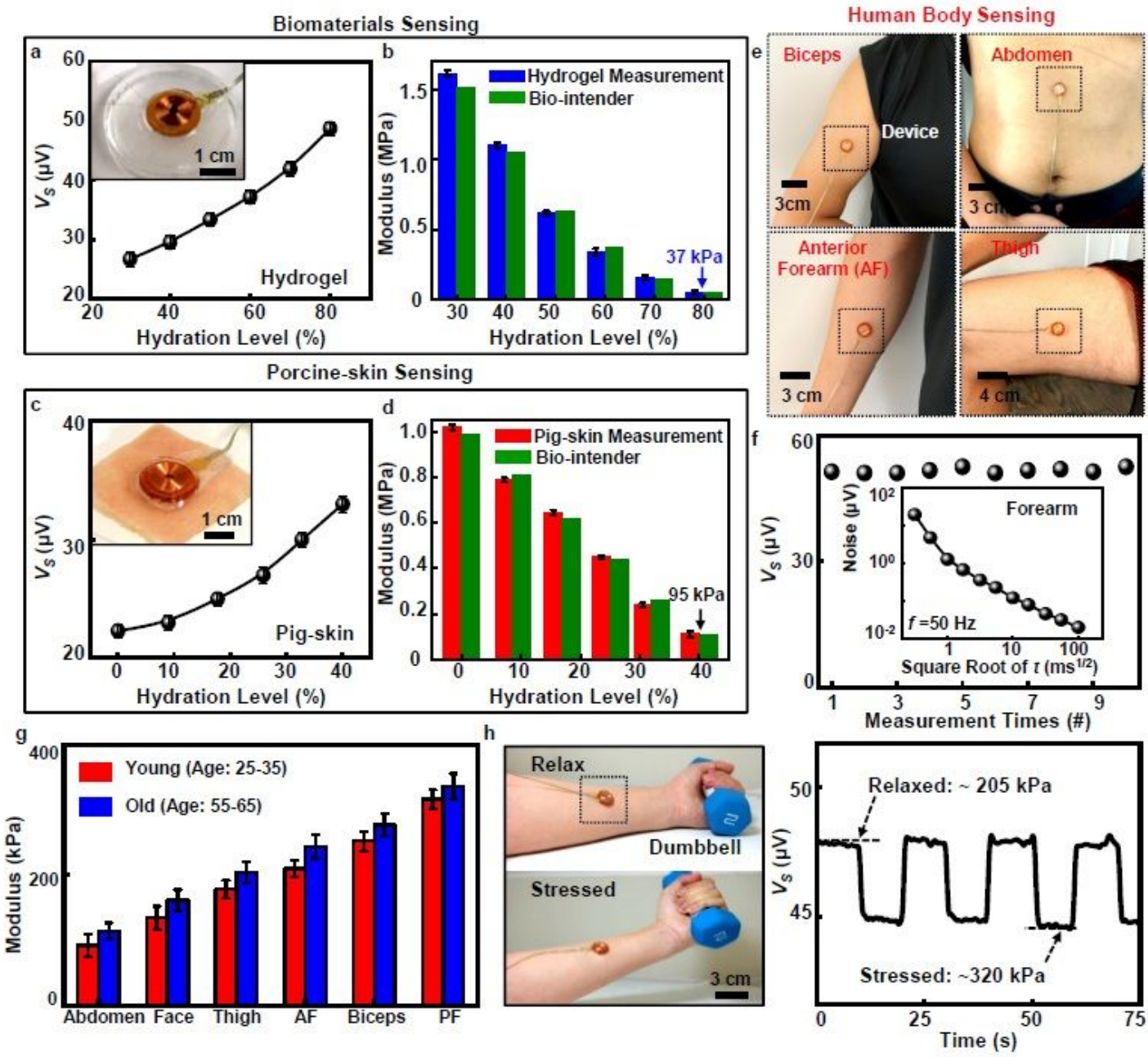

Figure 3

Modulus measurements on hydrogels and on porcine and human skin. (a) Vs as function of weight percentage of water of a hydrogel sample. Inset shows the device on a ~4 mm thick sample of hydrogel during measurements. (b) Modulus measured by an EMM sensor (blue) and values determined using a biosoft indenter (green), with various water content of the hydrogel. (c) Vs as function of weight percentage of water in porcine facial skin. Inset shows the device on a sample of porcine skin (2 mm thick). (d) Modulus measured by an EMM sensor (red) and indenter (green). (e) Photographs of devices on different locations of the human body. (f) Repeatibility of measurements as a function of measurement time at the same location on the forearm. Inset shows the noise for a representative

measurement on the forearm as a function of the square root of the integration time (t) configured on the lock-in amplifier. (g) Modulus measurements for different locations of the human body for each of ten subjects with young (red, age: 25-35) and old (cyan, age: 55-65), where the AF and PF correspond to the anterior and posterior forearm. Error bars correspond to the standard deviation for measurements among volunteer subjects. (h) Dynamic measurements for modulus sensing. Left: Photographs of the forearm before (upper) and after (lower) lifting a dumbbell. Right: Vs as function of time during signal recording at a sampling frequency of 5 Hz.

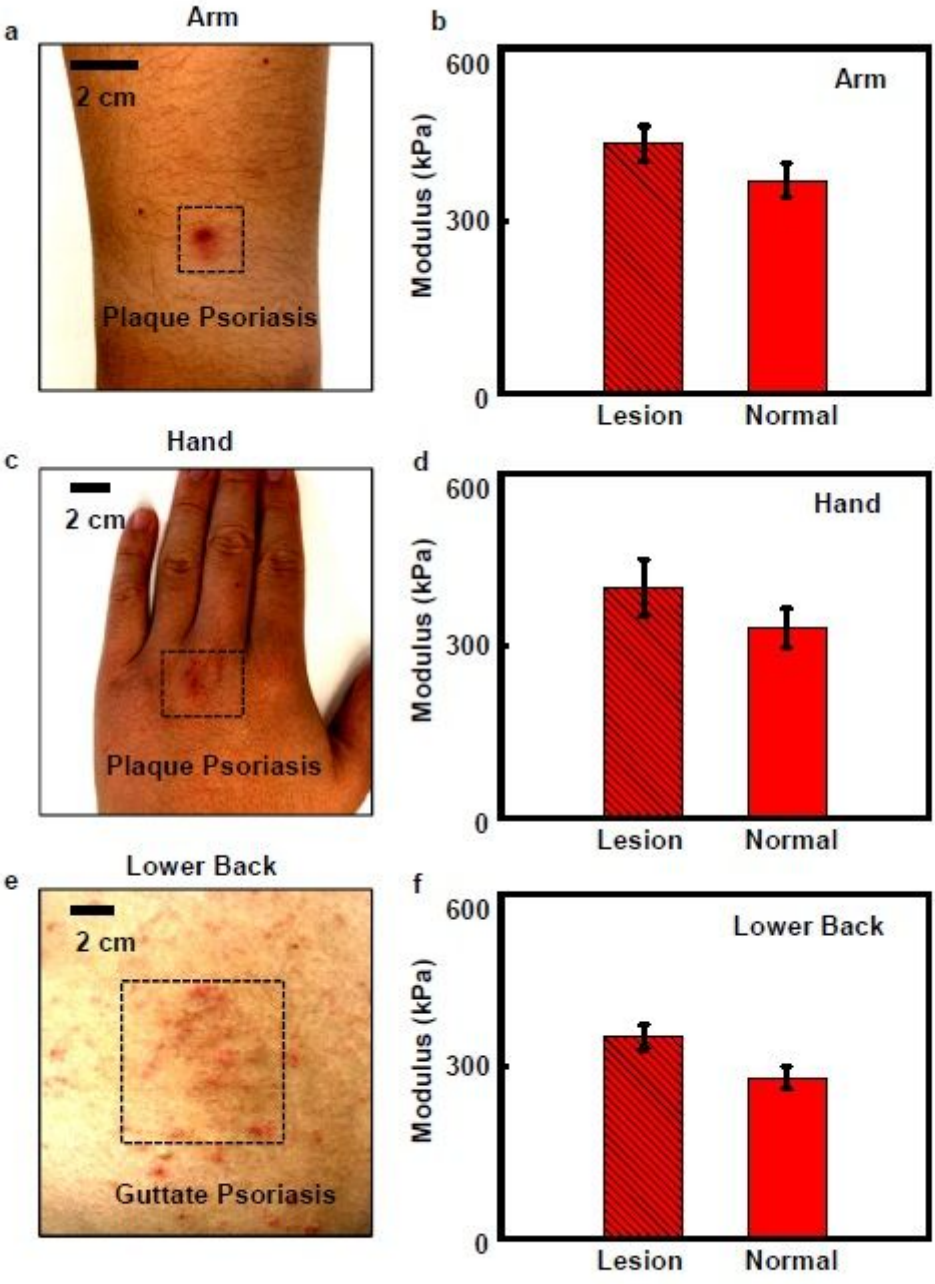

Figure 4

EMM sensor measurements of skin lesions located on various regions of patients. Photographs of skin lesions associated with psoriasis on the (a) arm, (c) hand and (e) lower back, with EMM measurements on the lesions and on nearby normal skin. The black frames correspond to the lesions, including symptoms of plaque psoriasis, Guttate psoriasis, etc. (b), (d), (f) Measurement results for the modulus values of lesions and nearby normal skin, collected in (a), (c) and (e), respectively.

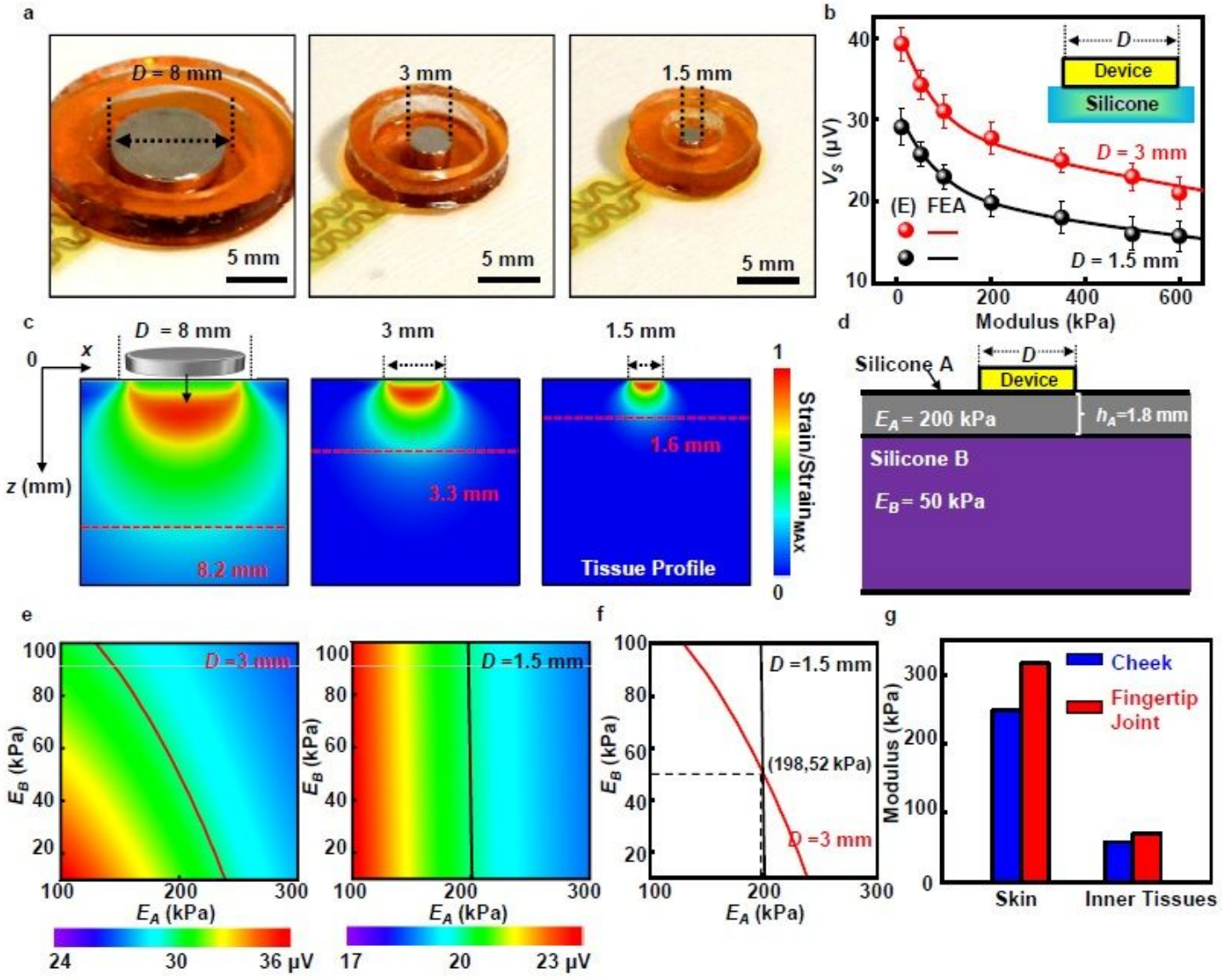

Figure 5

Designs for modulus sensing and depth profiling of multilayer samples. (a) Photograghs of devices with various sensing areas. (b) Simulated (FEA, line) and measured (E, symbols) Vs for systems with different dimensions as a function of elastic modulus for artificial skin samples. D corresponds to the sensing diameter of the EMM sensor. (c) Normalized FEA results for distributions of strain throughout the tissue structure with 200 kPa, shown in cross-sectional profile during actuator vibration, with different D. z is the

depth into the tissue and x corresponds to the direction along the surface. The effective saturation depths decrease with decreasing D from 8 mm to 1.3 mm. (d) Schematic illustration of a bilayer structure that approximates the skin/tissue system, with modulus values of 200 kPa and 50 kPa, and with thicknesses of 1.8 mm and >>1 cm, for the top and bottom layers respectively. (e), (f) FEA modeling to determine the modulus of each layer in the bilayer structure from measurements using EMM sensors with different D (e), yielding simulation results for EA and EB in (f). (g) Simulated results of moduli for the skin and underlying tissues of the cheek and fingertip joint of a human subject.

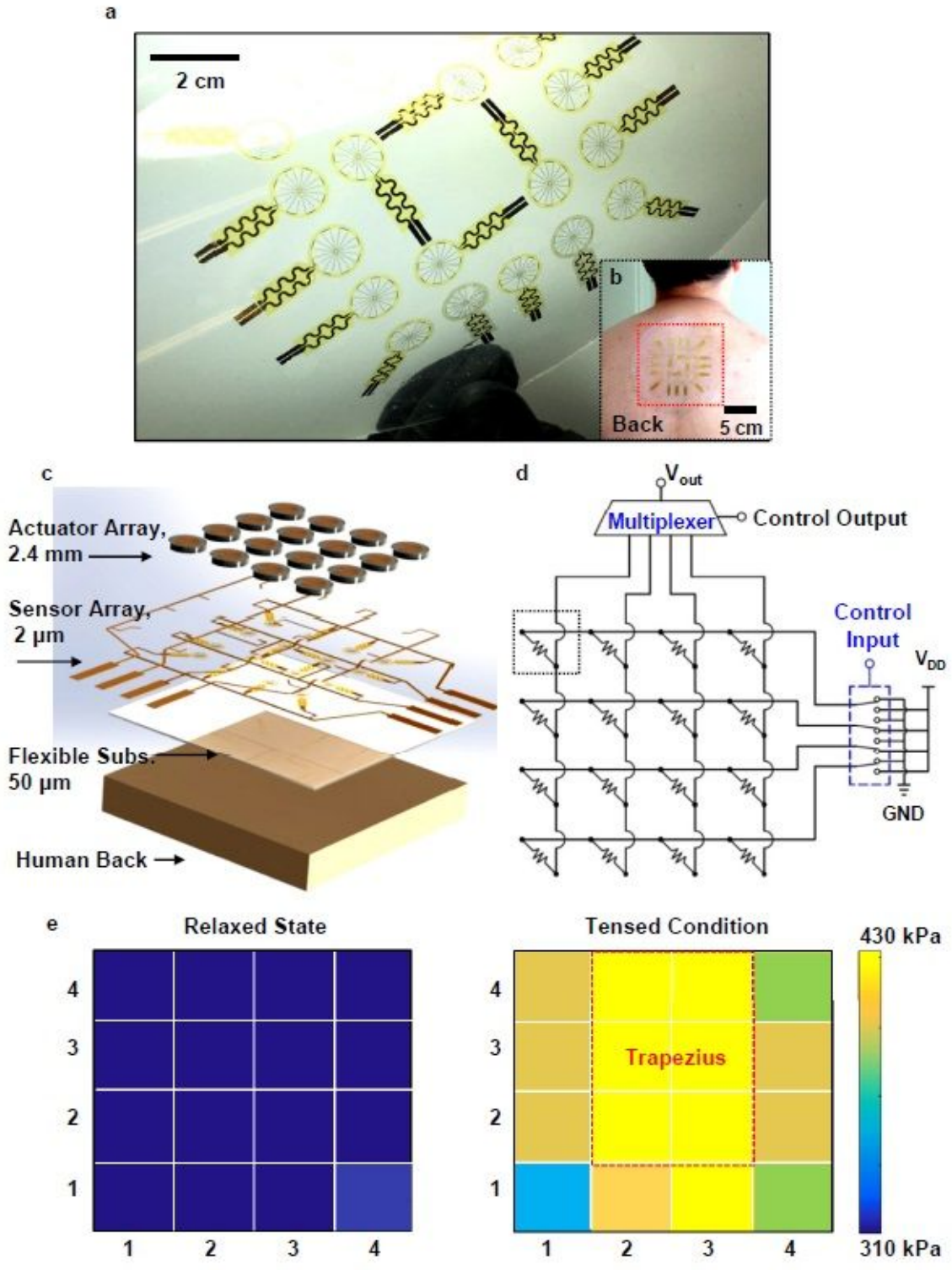

Figure 6

Multiplexed arrays of EMM sensors for spatial mapping of tissue modulus. (a) Photographs of a collection of strain sensors printed on a thin film of PDMS. (b) Photograph of the sensor array laminated onto the back of a volunteer human subject. The red frame highlights the device area. (c) Exploded-view schematic illustration of the layer configuration of a 4 × 4 array of sensors. The black frame corresponds to a unit cell. (d) Schematic diagram of the multiplexing circuit for the array mapping system. (e) Large-area spatial mapping of modulus obtained with this system while mounted on the back during a relaxed state (left) and tensed condition (right). Red frame corresponds to the estimated location of the trapezius muscles.

Supplementary Files

This is a list of supplementary files associated with this preprint. Click to download.

- MovieS1.mp4
- RogersRSf.pdf
- EnmingSong3206RogersCONSORTChecklist.doc
- EnmingSong3206RogersSupplementaryInformation.pdf